Supplement of Hydrol. Earth Syst. Sci., 30, 5215–5227, 2026
https://doi.org/10.5194/hess-30-5215-2026-supplement

Hydrology and Earth System Sciences
Open Access

Supplement of

Progressive groundwater decoupling may drive a shift toward shallower and faster terrestrial water cycling

Aoqi Sun et al.

Correspondence to: Chen Yang (yangch329@mail.sysu.edu.cn)

Supplementary Information

Text S1.

ParFlow (Kuffour et al., 2020; Maxwell, 2013; Kollet and Maxwell, 2006)solves variably saturated subsurface flow with the mixed form of Richards' equation and two-dimensional overland flow with the kinematic-wave approximation.

Richards' equation

$$S_s\,S(\psi)\,\frac{\partial\psi}{\partial t}+\phi\,\frac{\partial S(\psi)}{\partial t}=\nabla\cdot\boldsymbol{q}+q_s \qquad (S1)$$

$$\boldsymbol{q}\;=-\mathbf{K}_s\,k_r(\psi)\,\nabla(\psi-z) \qquad (S2)$$

where ψ is the pressure head $[L]$, $S(\psi)$ is the relative saturation, S_s is the specific storage coefficient $[L^{-1}]$, ϕ is porosity, $\boldsymbol{q}$ is the specific volumetric (Darcy) flux $[L\,T^{-1}]$, $\mathbf{K}_s$ is the saturated hydraulic conductivity tensor $[L\,T^{-1}]$, $k_r(\psi)$ is the relative permeability, z is depth below the surface [L], and q_s is a source/sink term $[T^{-1}]$. The non-linear relations $S(\psi)$ and $k_r(\psi)$ follow the van Genuchten-Mualem model.

Overland flow

$$\frac{\partial\psi_s}{\partial t}=\nabla\cdot(\mathbf{v}\,\psi_s)+q_r(x)+q_e(x) \qquad (S3)$$

with Manning's equation supplying the depth-averaged velocity components:

$$v_x=-\frac{\sqrt{S_{f,x}}}{n}\,\psi_s^{\frac{2}{3}},\qquad v_y=-\frac{\sqrt{S_{f,y}}}{n}\,\psi_s^{\frac{2}{3}} \qquad (S4)$$

where ψ_s is the surface ponding depth $[L]$, $\mathbf{v}=(v_x,v_y)$ is the depth-averaged velocity $[L\,T^{-1}]$, q_r is the rainfall flux $[L\,T^{-1}]$, q_e is the subsurface-surface exchange flux $[L\,T^{-1}]$, $S_{f,i}$ is the friction slope (set equal to the bed slope under the kinematic-wave assumption), and n is Manning's roughness coefficient.

EcoSLIM (Yang et al., 2023; Maxwell et al., 2019)is an open-source Lagrangian particle-tracking model that calculates the advection and molecular diffusion of water parcels in the subsurface based on the transient three-dimensional velocity field generated by ParFlow-CLM. The position of a particle in the subsurface is described as(Tompson and Gelhar, 1990; Tompson and Dougherty, 1988):

$$\mathbf{S}(t+\Delta t)-\mathbf{S}(t)=\mathbf{A}\,\Delta t+\mathbf{B}\cdot\mathbf{Z}\sqrt{\Delta t} \qquad (S5)$$

$$\mathbf{A}\equiv\mathbf{v}+\nabla\cdot\mathbf{D}+\frac{\mathbf{D}}{\phi\,\theta}\cdot\nabla(\phi\,\theta) \qquad (S6)$$

$$\mathbf{B}\cdot\mathbf{B}^T\equiv 2\,\mathbf{D} \qquad (S7)$$

where $\mathbf{S}(t)$ is the position vector of the particle at time t $[L]$, Δt is the local timestep of the particle $[T]$, $\mathbf{Z}$ is a vector of pseudorandom numbers, $\mathbf{v}$ is the velocity vector at time t $[L\,T^{-1}]$, $\mathbf{D}$ is the hydrodynamic dispersion tensor $[L^2\,T^{-1}]$, ϕ is the porosity, and θ is the saturation. The number density of particles $p(\mathbf{S}, t)$ satisfies the Ito-Fokker-Planck approximation:

$$\frac{\partial p}{\partial t} + \nabla \cdot (\mathbf{A}\,p) - \Delta\left(\frac{1}{2}\,\mathbf{B}\cdot\mathbf{B}^T\,p\right) = 0 \qquad (S8)$$

EcoSLIM determines the position of a water parcel by neglecting the macrodispersion in the equations above, yielding the advection-molecular-diffusion form actually solved in the code:

$$\mathbf{S}(t+\Delta t) - \mathbf{S}(t) = \mathbf{v}\,\Delta t + \mathbf{Z}\sqrt{2\,D_m\,\Delta t} \qquad (S9)$$

where D_m is the molecular diffusion coefficient $[L^2\,T^{-1}]$. Particles are dynamically added into the modeling domain where precipitation minus ET is positive (PME > 0). They move in the subsurface until they exit the domain as outflow (when they reach the stream bottom) or as ET (where PME < 0). Travel/residence times of outflow, ET, and groundwater are obtained by aggregating the travel times of the corresponding particles, and source composition is recovered by labeling particles with their water sources (e.g., snow, rainfall, or initial water).

Table S1. Vegetation, subsurface hydraulic, and topographic parameter values defining the four hillslope configurations. All other vegetation parameters were retained at their default CLM settings.

Table S1. Hillslope configurations

Configuration	Vegetation	K_s (m h^{-1})	Porosity	α (m^{-1})	n	S_{res}	Slope
Reference	Evergreen needleleaf forest	0.05	0.20	1.0	2	0.20	0.10
Modified vegetation	Open shrublands	0.05	0.20	1.0	2	0.20	0.10
Modified hydraulic properties	Evergreen needleleaf forest	0.10	0.39	3.5	2	0.01	0.10
Reduced slope	Evergreen needleleaf forest	0.05	0.20	1.0	2	0.20	0.05

Table S2. Air temperature perturbations and maximum LAI values defining the four ET-forcing scenarios. Each hillslope configuration was simulated under all four forcing scenarios, yielding 16 model scenarios.

Table S2. ET forcing scenarios

Forcing scenario	Air temperature perturbation (°C)	Maximum LAI: forest	Maximum LAI: shrubland
Baseline	0	6	6
Warming	+1	6	6
Greening	0	9	9
Warming+Greening	+1	9	9

Figures S1–S10 correspond to the four forcing scenarios under the reference parameter set, whereas Figures S11–S16 present results from the three modified parameter sets.

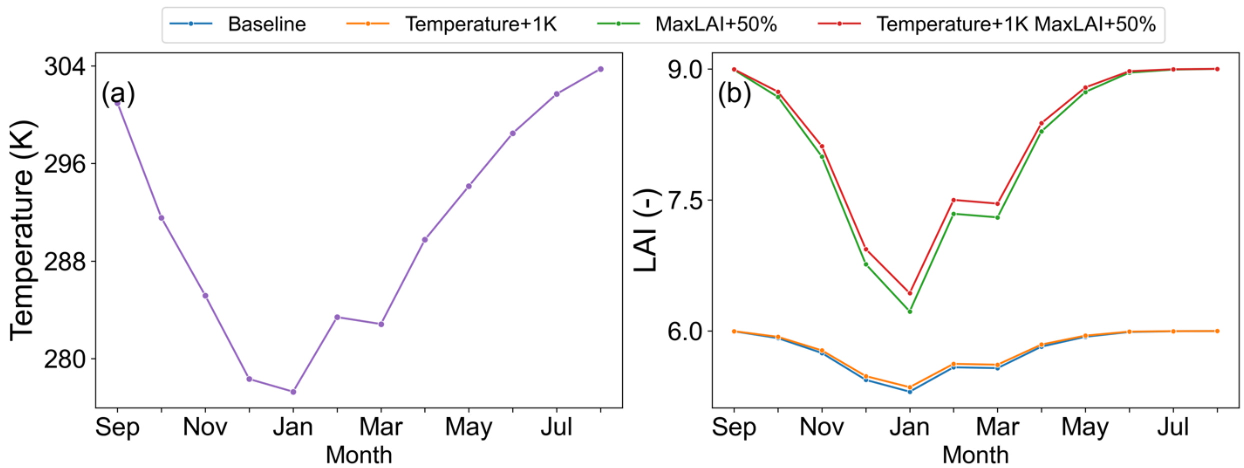

Figure S1. Monthly mean forcing conditions used in the four ET-forcing scenarios. (a) Air temperature and (b) leaf area index (LAI). The warming scenario increases air temperature uniformly by 1 °C throughout the year, while the greening scenario increases maximum LAI by 50%. The combined warming–greening scenario applies both perturbations simultaneously. Seasonal variations in temperature and vegetation activity are preserved across all scenarios, while the imposed perturbations enhance atmospheric and biological water demand.

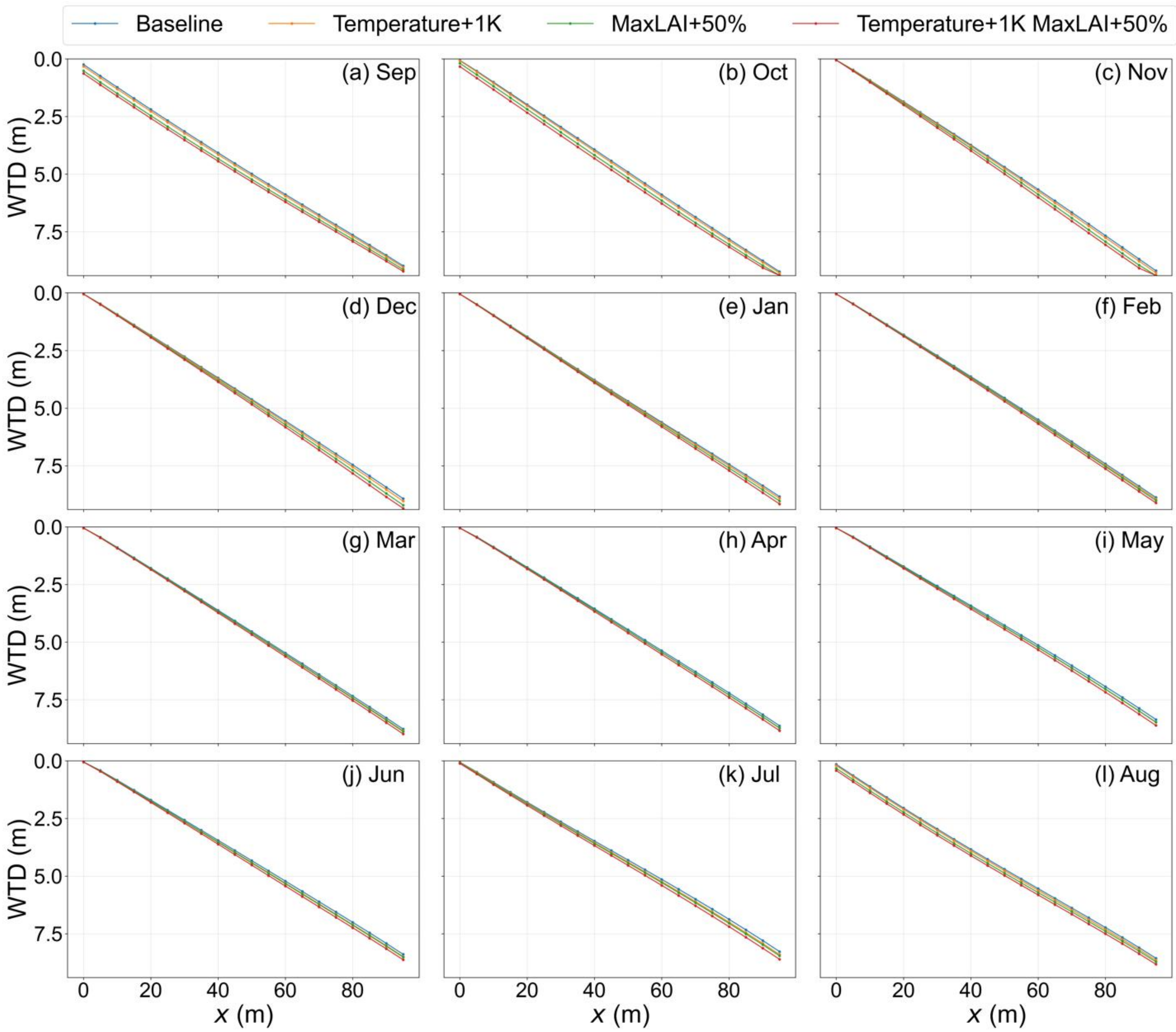

Figure S2. Seasonal evolution of water table depth (WTD) along the hillslope under the four ET-forcing scenarios. Enhanced ET forcing generally deepens the water table throughout the hillslope. In September, the water table near the hillslope outlet falls below the outlet elevation, indicating hydraulic disconnection between groundwater and the outlet. This disconnection coincides with the temporary loss of streamflow and the collapse of older-water contributions discussed in the main text.

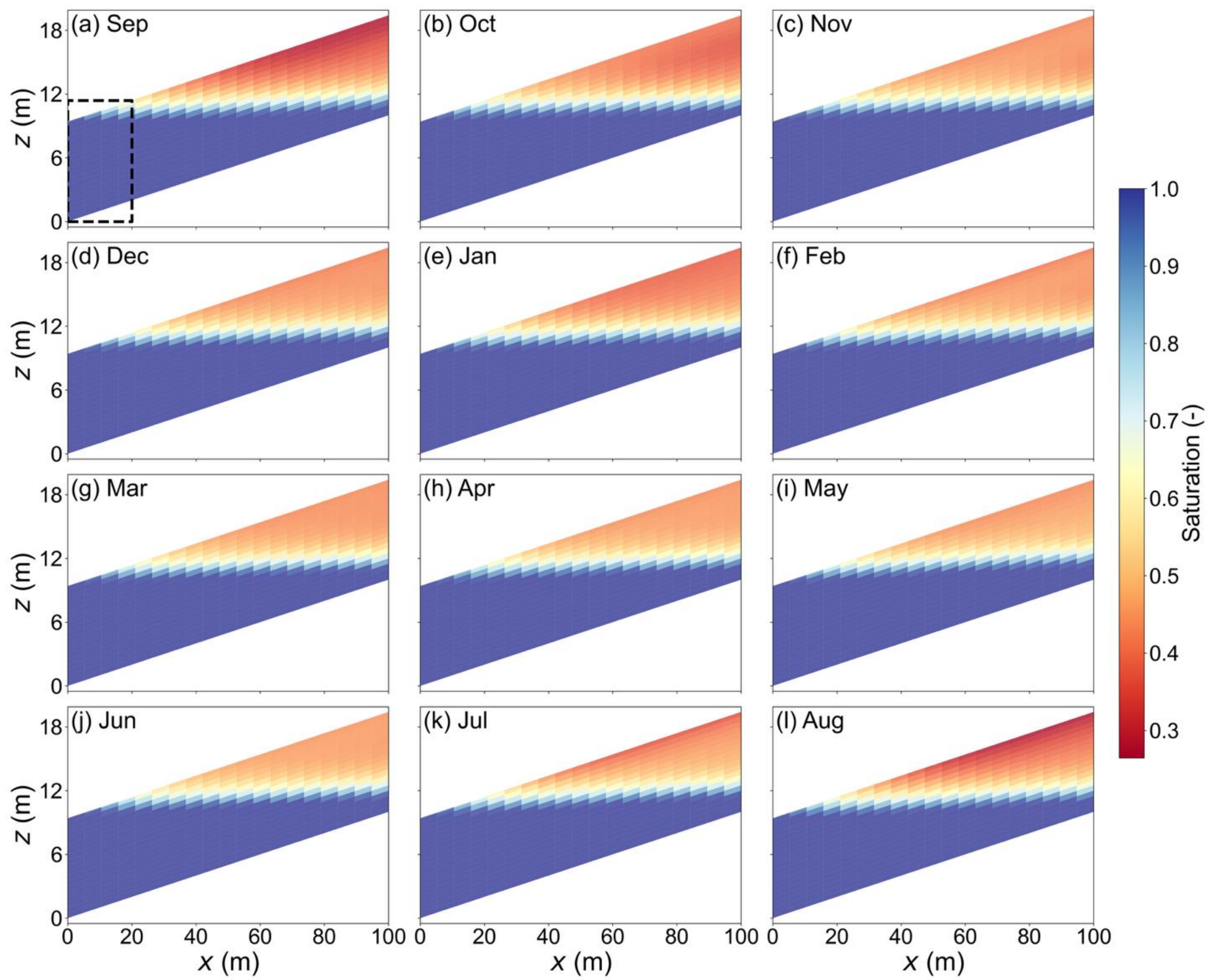

Figure S3. Seasonal evolution of hillslope saturation profiles under baseline conditions. Colors indicate saturation, with warmer colors representing drier conditions and cooler colors representing higher saturation. The dashed box highlights the lower 20 m section of the hillslope (x = 0–20 m) referred to in the main text. The saturation profiles show progressive drying and water-table decline during the late growing season (July–September), followed by gradual recovery during autumn, winter, and spring.

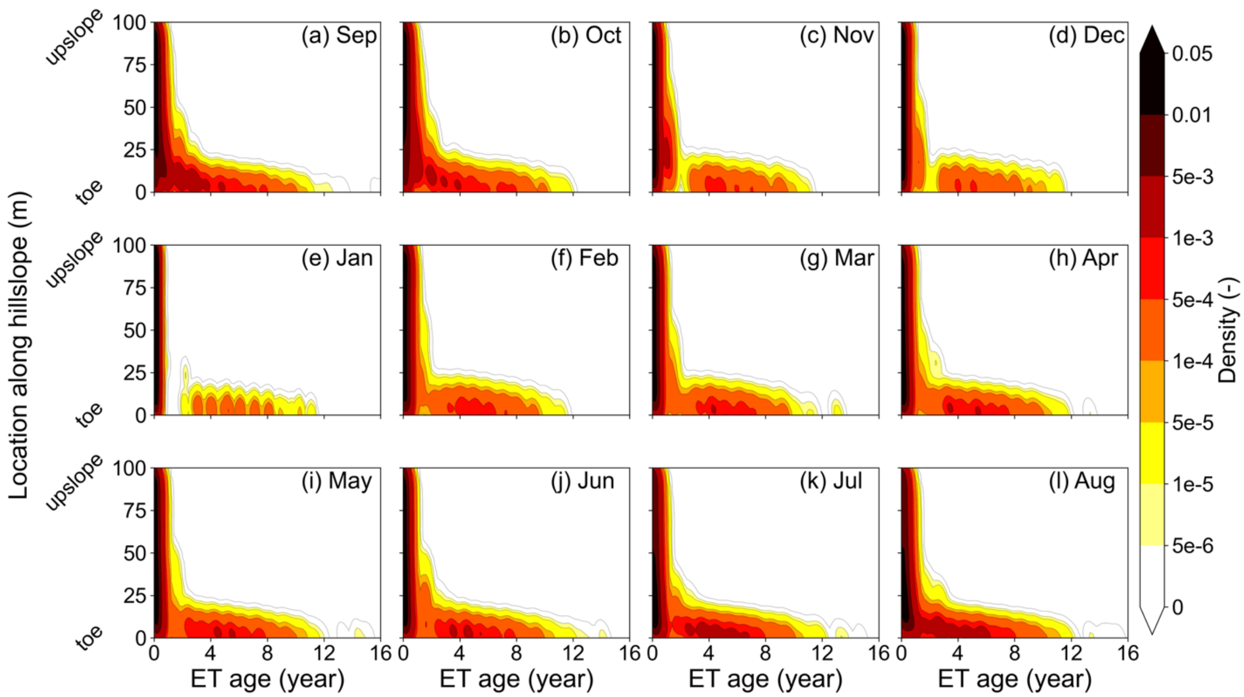

Figure S4. Seasonal evolution of ET age distributions along the hillslope under the warming scenario (+1 °C). Compared with the baseline case (Figure 4), warming promotes stronger depletion of intermediate-age contributions during winter and enhances the seasonal separation between younger and older ET age components.

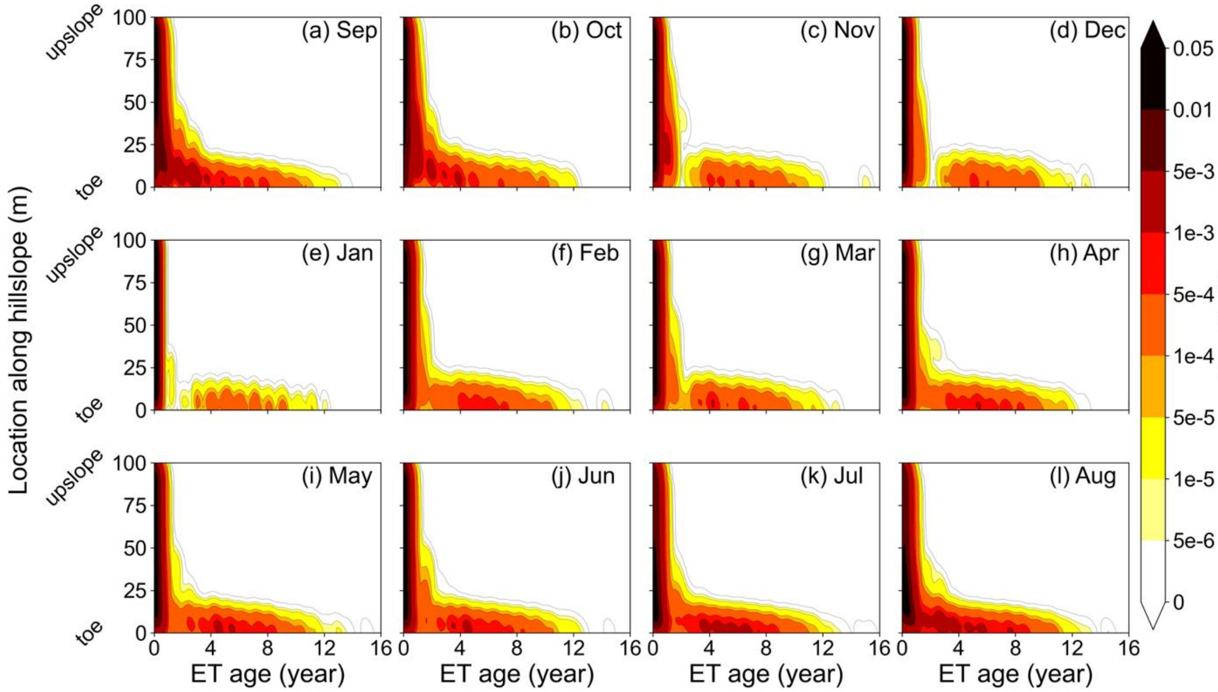

Figure S5. Seasonal evolution of ET age distributions along the hillslope under the greening scenario (MaxLAI +50%). Increased vegetation water demand enhances the depletion of intermediate-age contributions during winter, resulting in stronger seasonal age segregation compared with the baseline case (Figure 4).

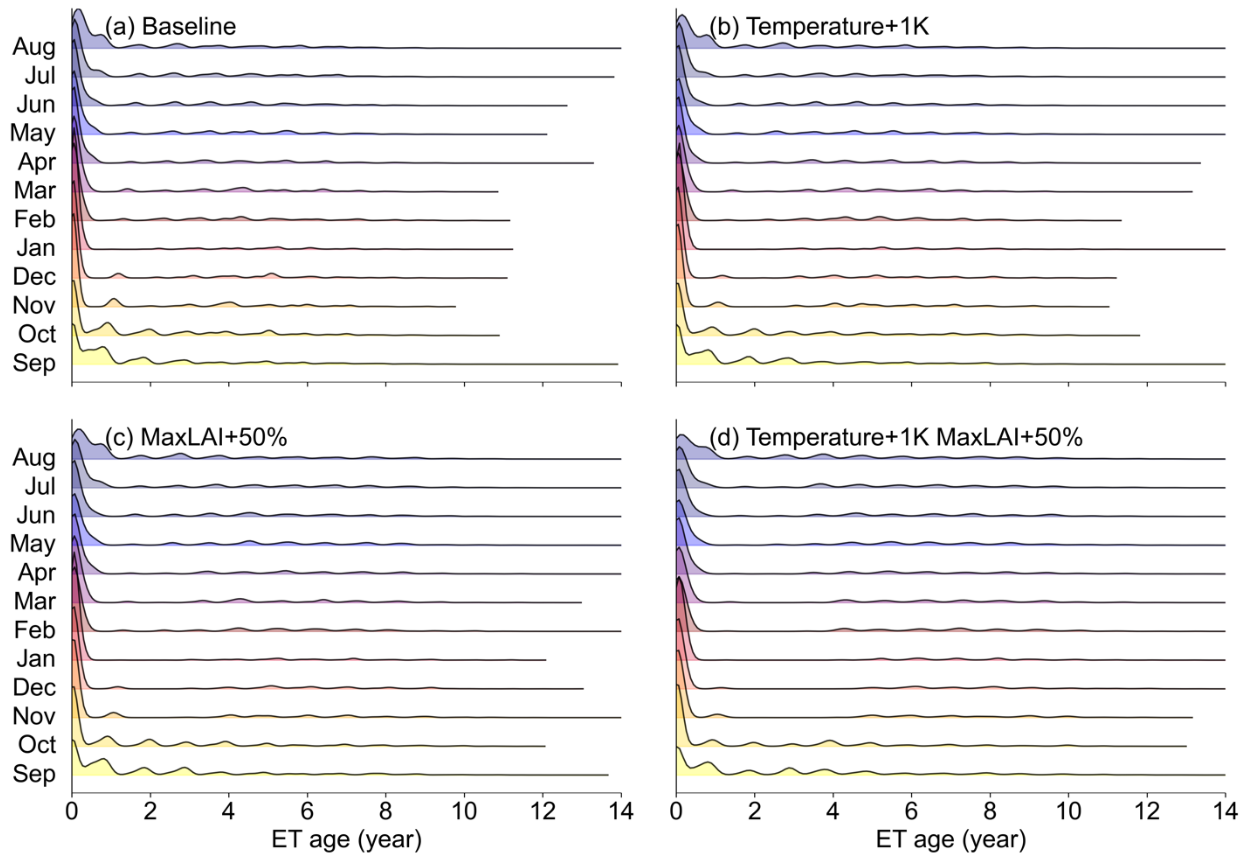

Figure S6. Seasonal ET age distributions within the lower 20 m section of the hillslope under the four ET-forcing scenarios. Compared with Figures 4, 5, S4, and S5, the spatial information is aggregated to highlight the age structure of ET source waters within the downslope zone. Despite the loss of spatial detail, the seasonal age gap remains clearly visible during winter (particularly in January), characterized by a marked depletion of intermediate-age contributions and only weak contributions from the oldest water components. Relative to the baseline case, enhanced ET forcing produces a wider age gap and stronger age polarization.

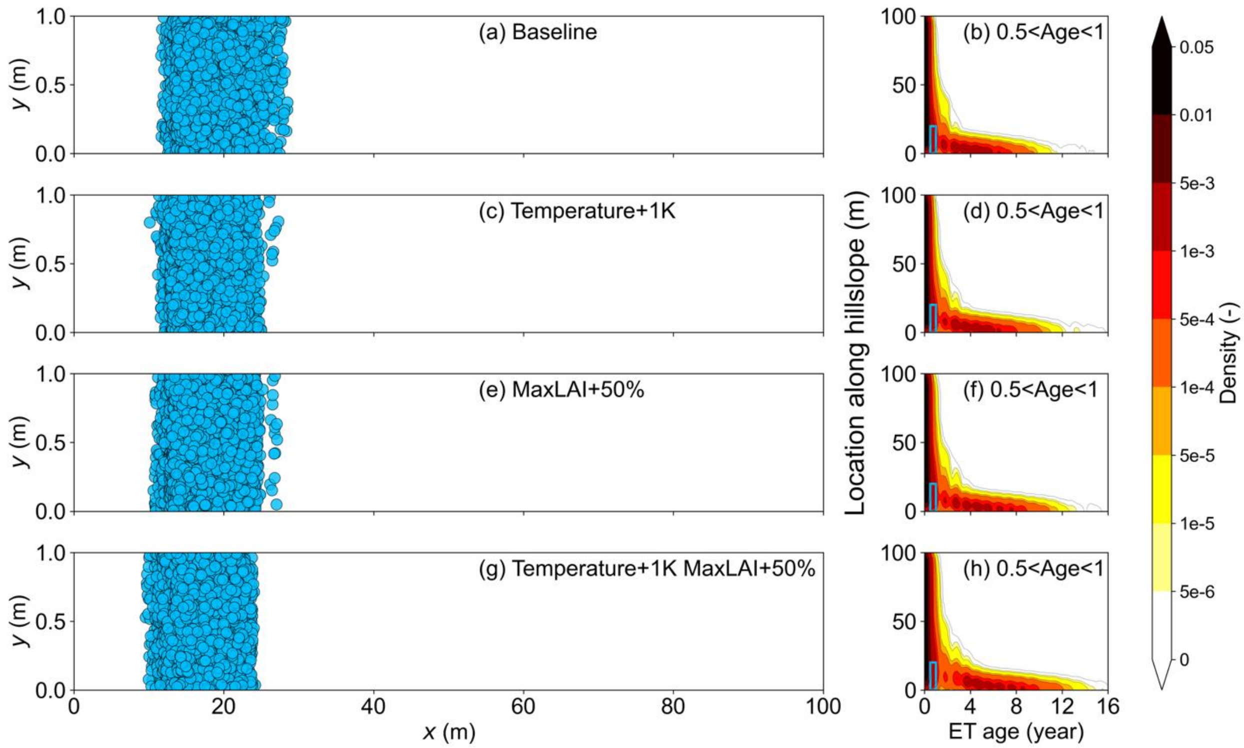

Figure S7. Source locations of ET particles with ages between 0.5 and 1 year contributing to annual ET within the downslope 20 m section of the hillslope under the four ET-forcing scenarios. Left panels show the inferred source locations of the selected particles in the x–y domain, while right panels show the corresponding ET age distributions as a function of distance along the hillslope. Blue rectangles indicate the selected age interval used to identify the particle populations shown in the left panels. Across all scenarios, these young ET particles originate predominantly from shallow and local source regions near the hillslope outlet, consistent with the dominance of rapidly recycled water in the young-age component.

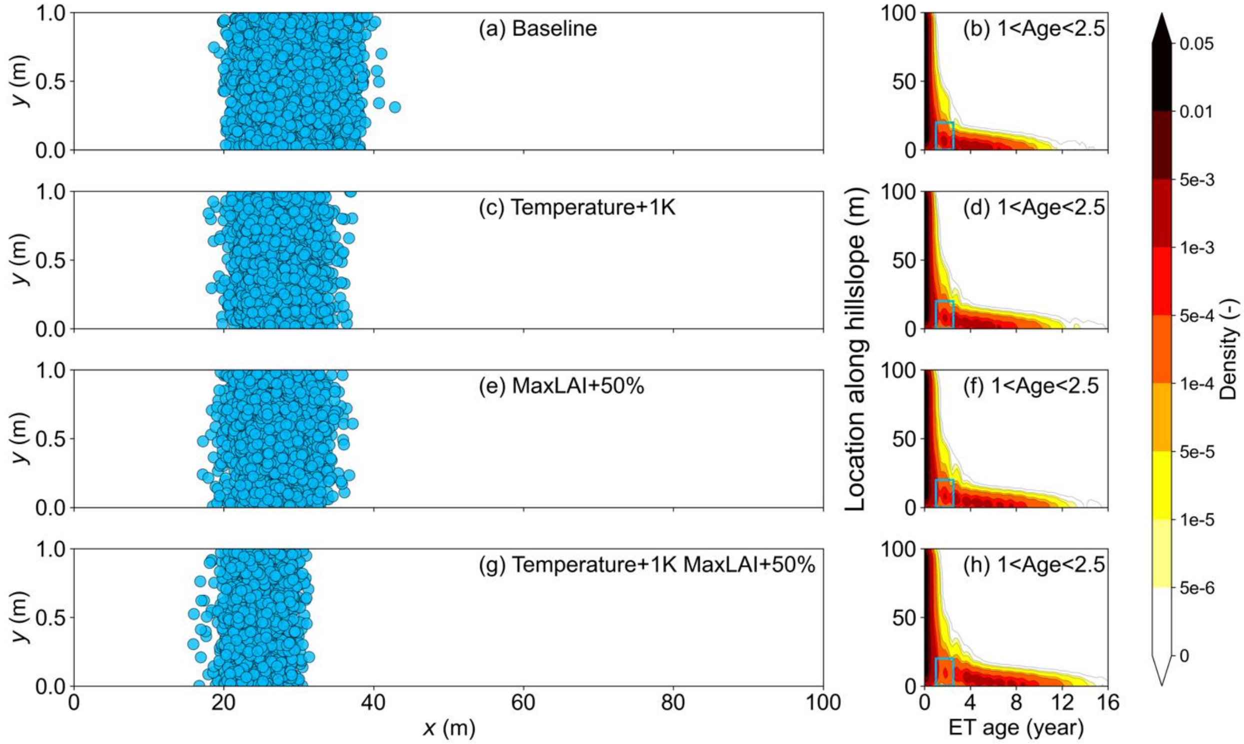

Figure S8. Source locations of ET particles with ages between 1 and 2.5 years contributing to annual ET within the downslope 20 m section of the hillslope under the four ET-forcing scenarios. Left panels show the inferred source locations of the selected particles in the x–y domain, while right panels show the corresponding ET age distributions as a function of distance along the hillslope. Blue rectangles indicate the selected age interval used to identify the particle populations shown in the left panels. Compared with the younger age class shown in Figure S7, these particles originate from more upslope locations, indicating that the older ET age component in the downslope zone is supplied by more distal subsurface storage rather than purely local recharge.

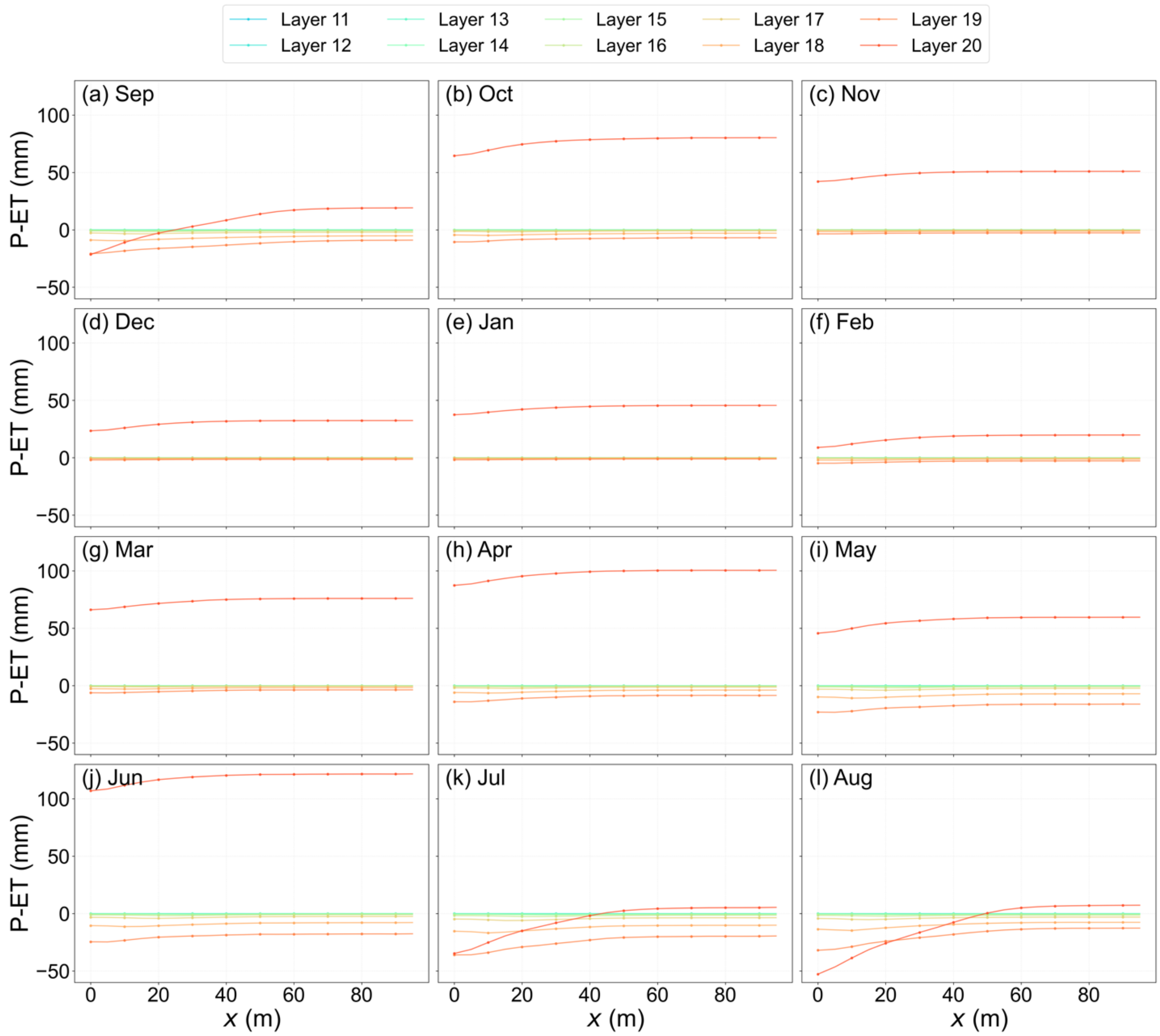

Figure S9. Monthly along-slope distribution of P–ET across root-zone layers under baseline forcing. Layers 11–20 are ordered from bottom to top within the root zone, with Layer 20 representing the uppermost root-zone layer. Positive values indicate net water gain (P > ET), whereas negative values indicate net water loss (ET > P). Most lower root-zone layers exhibit relatively small net fluxes throughout the year, while the uppermost root-zone layer (Layer 20) accounts for the majority of the seasonal water surplus and deficit. Positive P–ET during autumn, winter, and spring indicates recharge and storage recovery, whereas negative P–ET during late summer reflects enhanced water extraction and storage depletion.

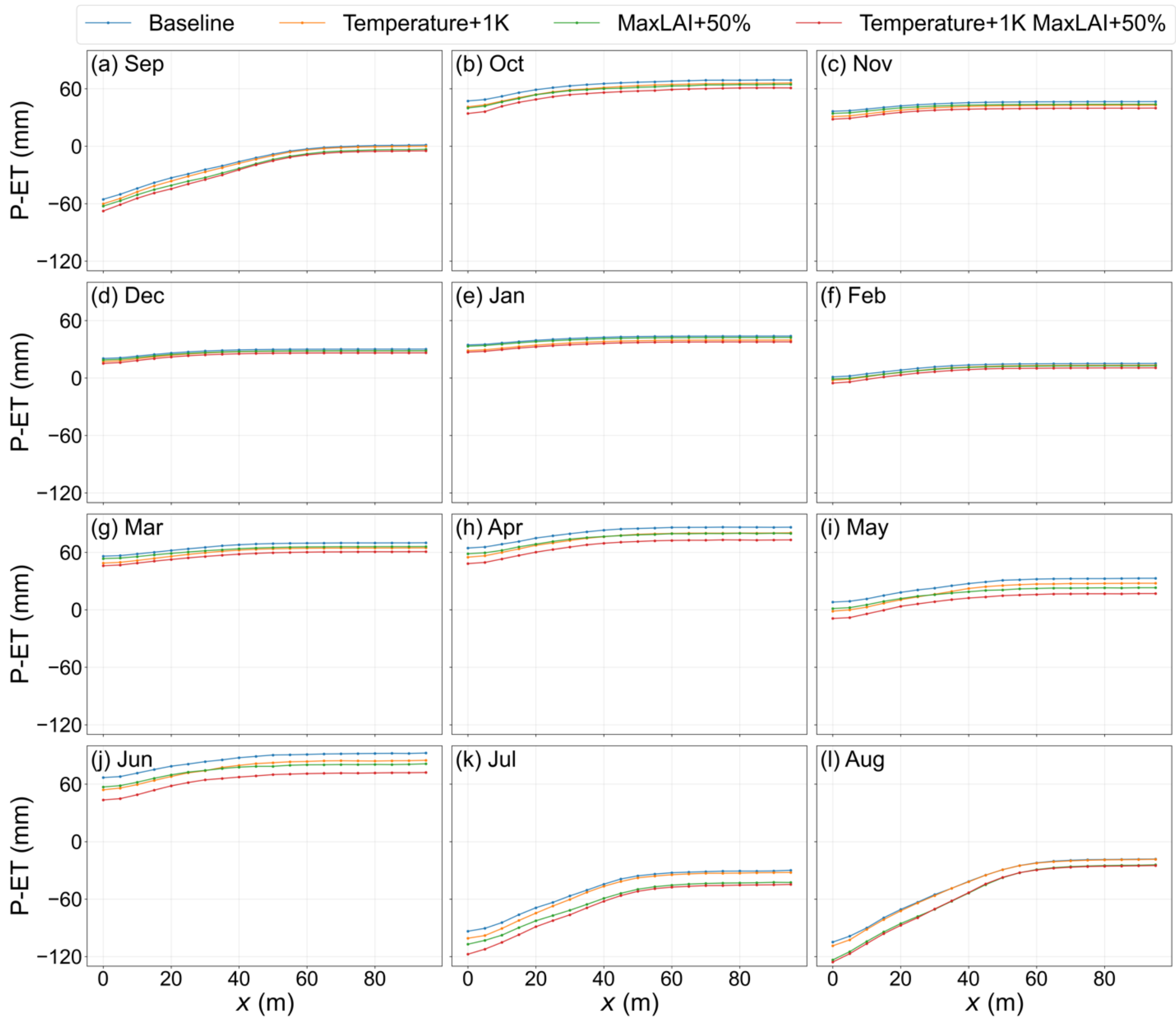

Figure S10. Monthly root-zone P–ET distribution along the hillslope under the four ET-forcing scenarios. Positive values indicate net water gain (P > ET), whereas negative values indicate net water loss (ET > P). The root zone experiences net recharge during autumn, winter, and spring and net water deficits during late summer. Enhanced ET forcing generally reduces recharge surpluses and intensifies summer deficits, indicating greater seasonal depletion of subsurface water storage under warming and greening conditions.

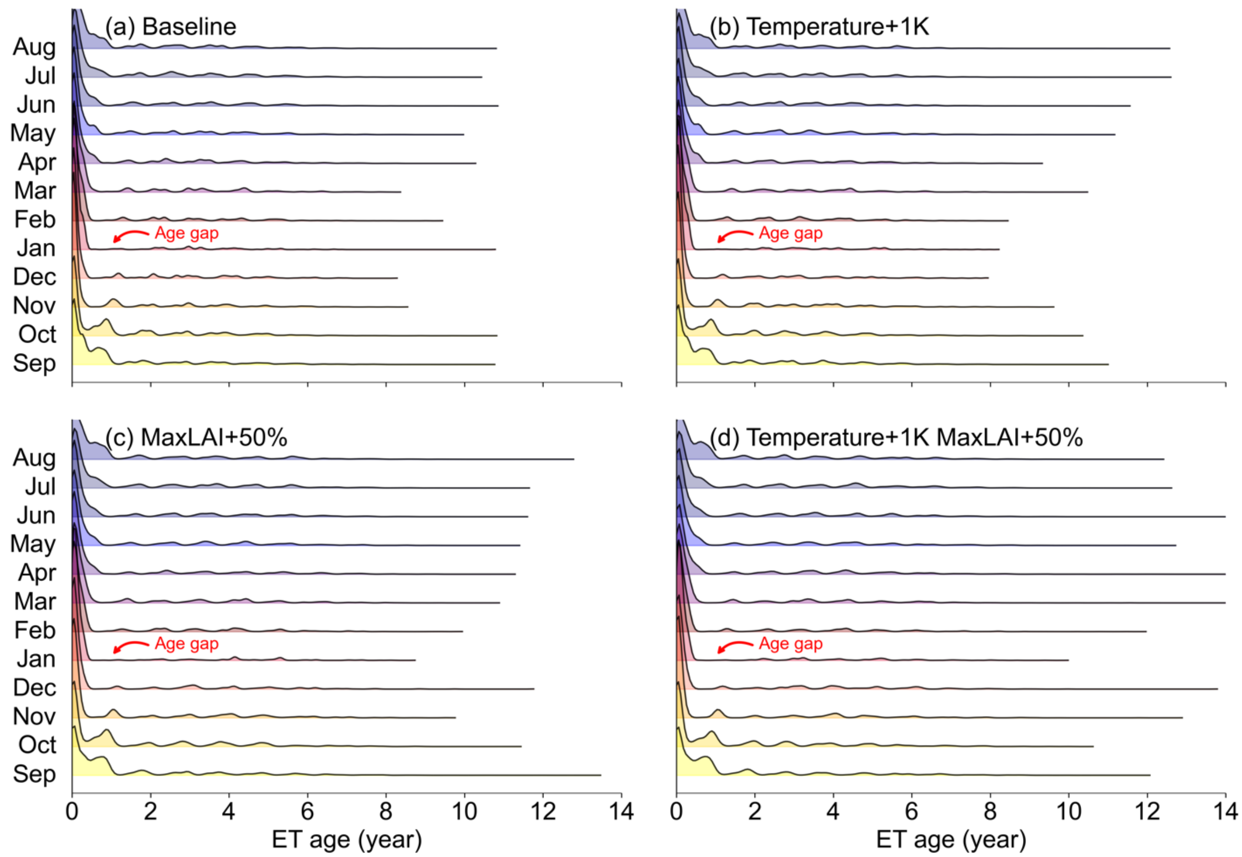

Figure S11. Seasonal ET age distributions within the lower 20 m section of the hillslope under shrub vegetation. Compared with the tree-covered reference configuration (Figure S6), reduced vegetation water demand weakens the seasonal depletion of intermediate-age contributions and results in a narrower age gap. Nevertheless, the age gap remains detectable during winter months, indicating that connectivity-driven age segregation persists despite reduced hydrologic stress.

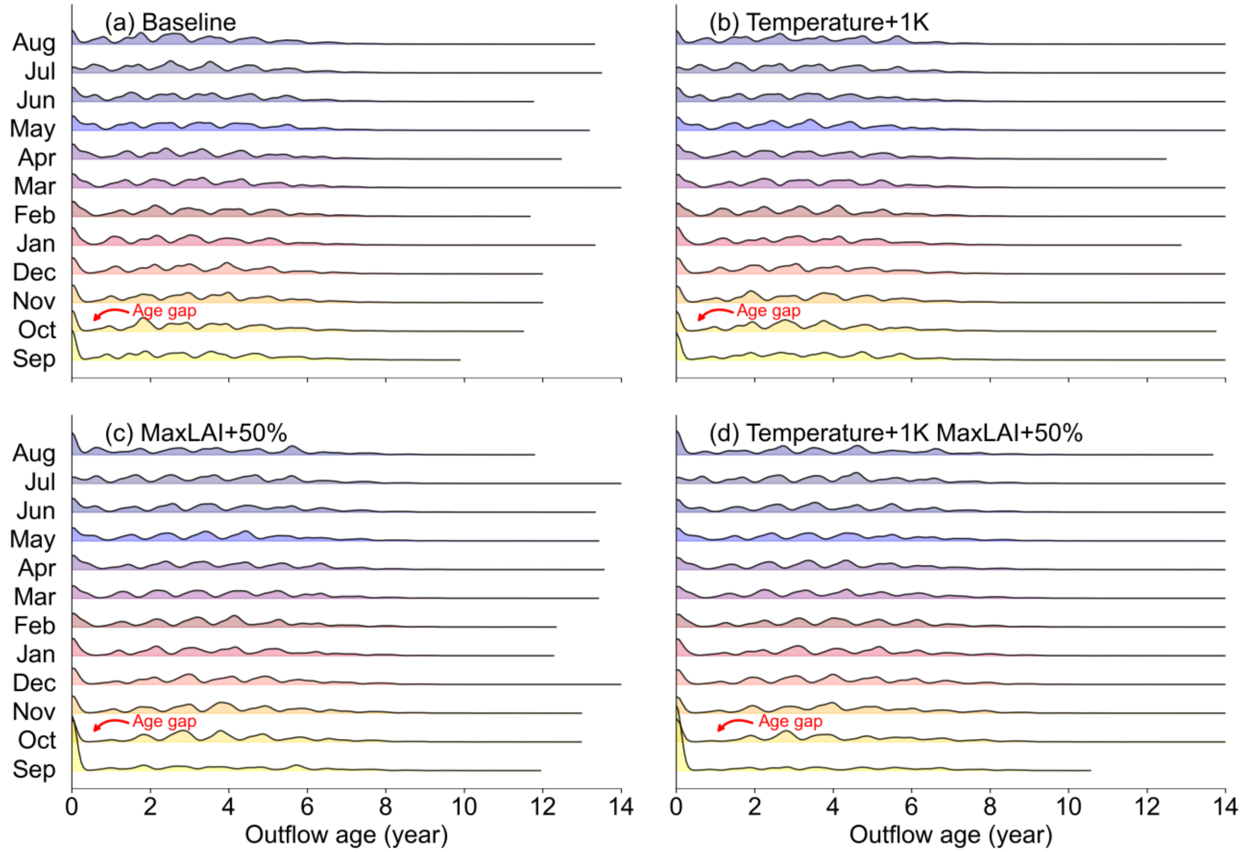

Figure S12. Seasonal outflow age distributions under shrub vegetation. Compared with the tree-covered reference configuration (Figure 6), reduced ET demand weakens seasonal age polarization and diminishes the magnitude of the age gap. However, the separation between younger and older outflow age components remains evident, demonstrating that the underlying reorganization pattern persists under lower vegetation water demand.

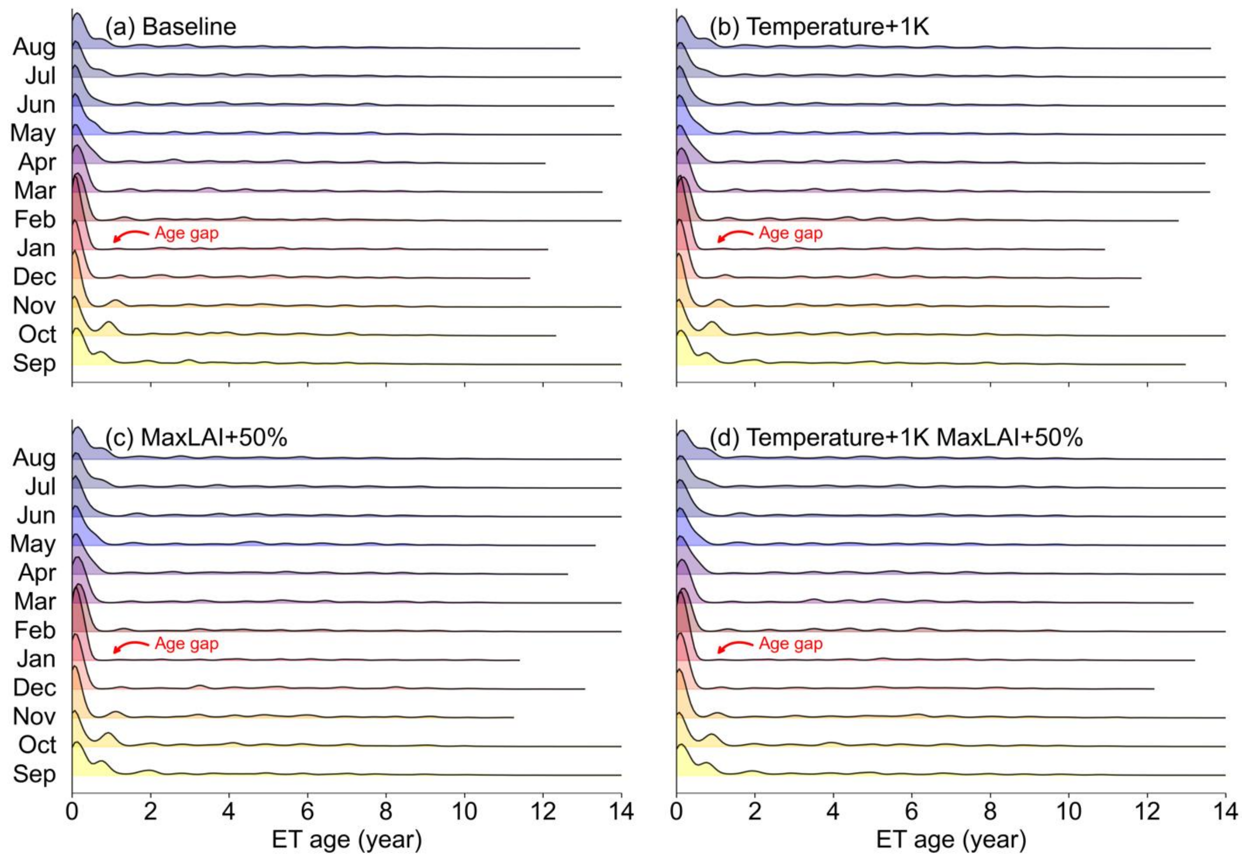

Figure S13. Seasonal ET age distributions within the lower 20 m section of the hillslope under modified subsurface hydraulic properties. Relative to the reference configuration (Figure S6), the modified hydraulic properties weaken the depletion of intermediate-age contributions and reduce the degree of age polarization. Although the age gap remains detectable during winter months, it is substantially muted, indicating that altered hydraulic properties redistribute ET contributions across age classes and weaken, but do not eliminate, the underlying pattern of age-segregation.

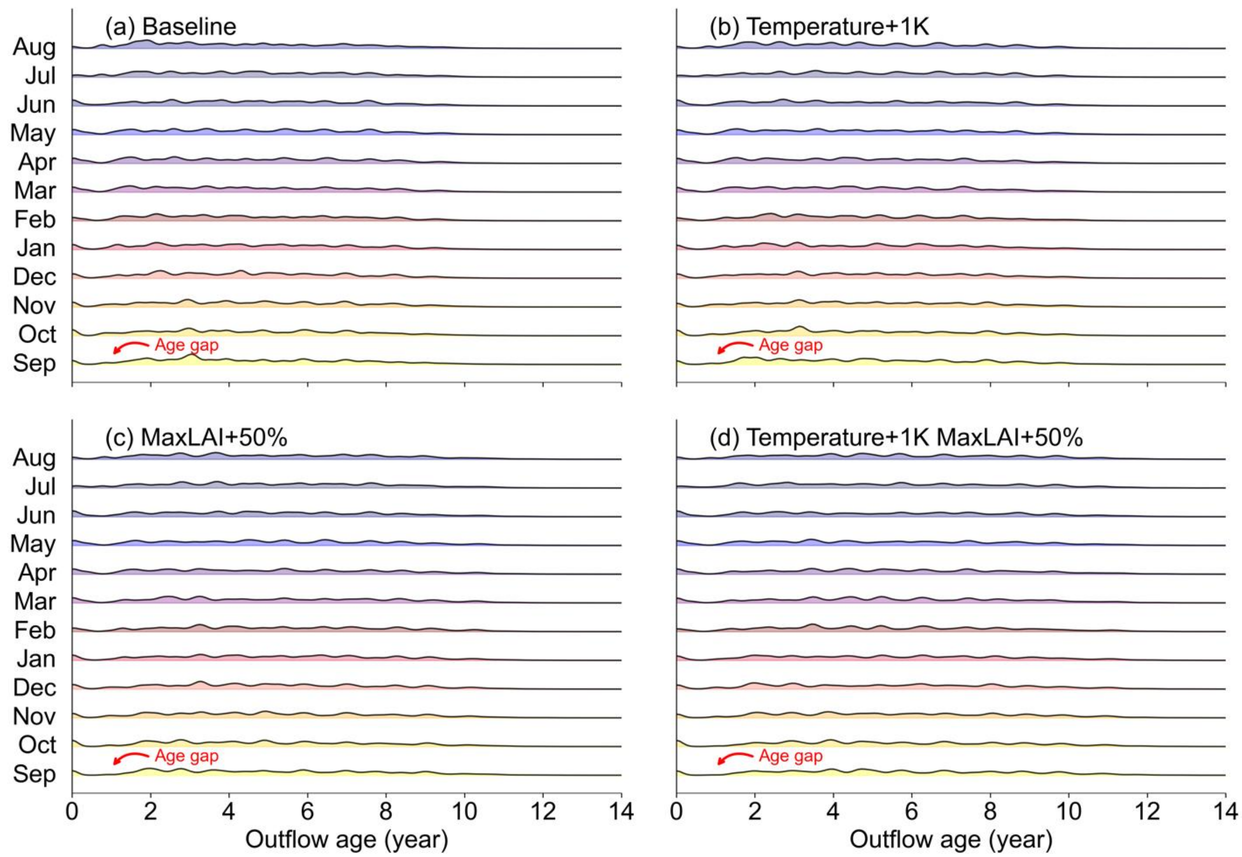

Figure S14. Seasonal outflow age distributions under modified subsurface hydraulic properties. Compared with the reference configuration (Figure 6), altered hydraulic properties increase the contribution of older water to outflow and weaken the seasonal age gap. The age gap remains identifiable but is considerably less pronounced, indicating that changes in hydraulic connectivity primarily redistribute the balance between young and old water contributions without eliminating the underlying pattern of age-segregation.

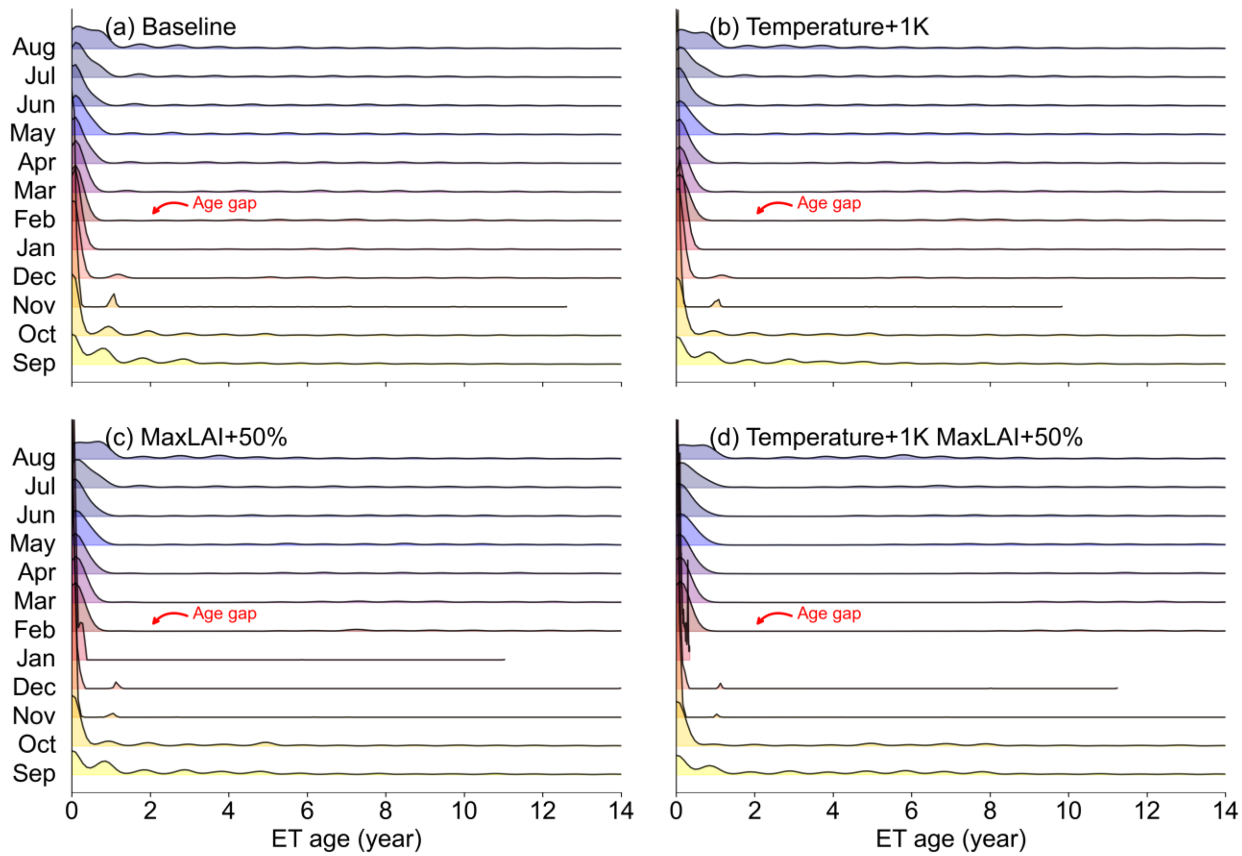

Figure S15. Seasonal ET age distributions within the lower 20 m section of the hillslope under reduced hillslope gradient. Relative to the reference configuration (Figure S6), weaker topographic control produces a substantially more pronounced age gap and stronger seasonal age segregation. During winter months, contributions from older ET water sources nearly disappear, leaving a clear separation between rapidly recycled young water and the remaining older age component. These patterns indicate enhanced seasonal decoupling under reduced hillslope gradient.

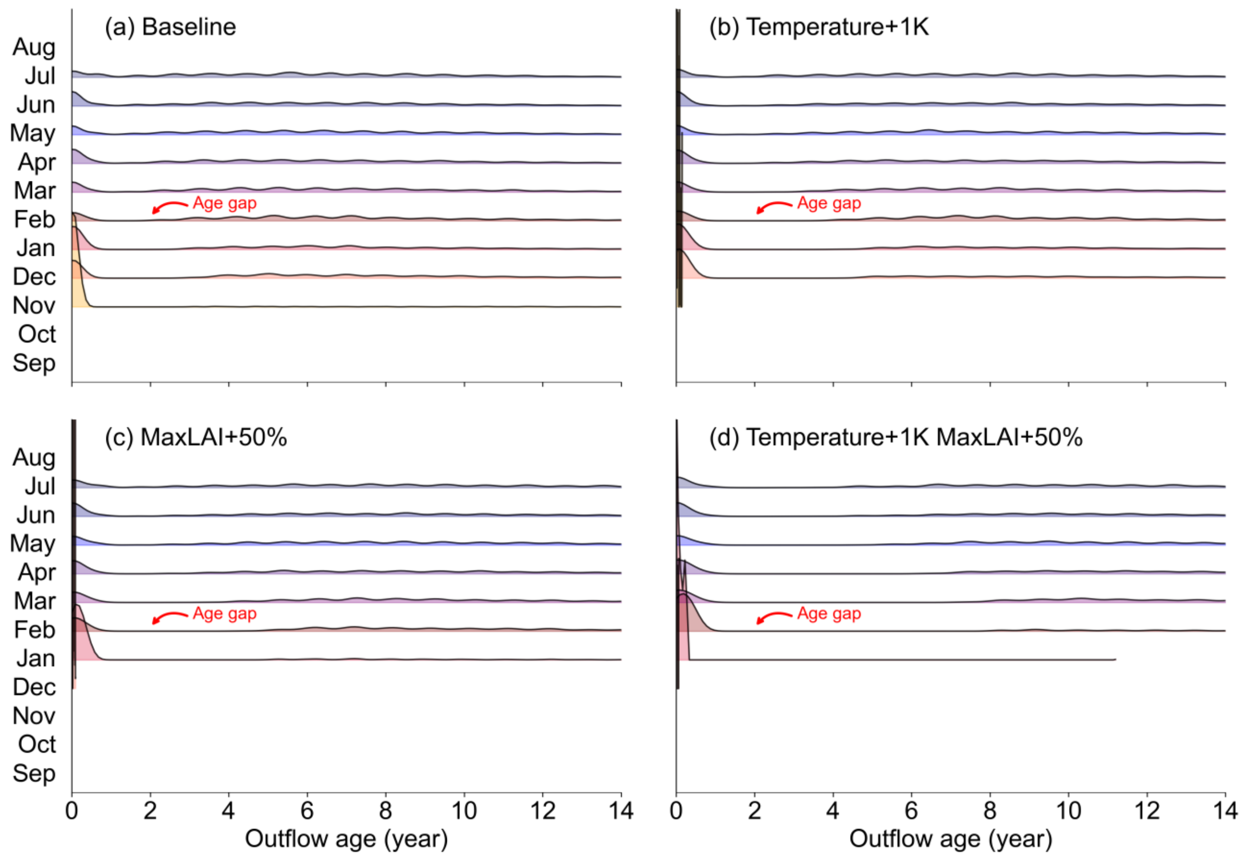

Figure S16. Seasonal outflow age distributions under reduced hillslope gradient. Compared with the reference configuration (Figure 6), reduced hillslope gradient strongly suppresses older-water contributions during winter months and produces a wider and more persistent age gap. The resulting age distributions are dominated by young water, indicating enhanced groundwater–surface decoupling and weaker hydraulic connectivity under reduced topographic forcing.

References

Kollet, S. J. and Maxwell, R. M.: Integrated surface-groundwater flow modeling: A free-surface overland flow boundary condition in a parallel groundwater flow model, Advances in Water Resources, 29, 945-958, https://doi.org/10.1016/j.advwatres.2005.08.006, 2006.

Kuffour, B. N. O., Engdahl, N. B., Woodward, C. S., Condon, L. E., Kollet, S., and Maxwell, R. M.: Simulating coupled surface–subsurface flows with ParFlow v3.5.0: capabilities, applications, and ongoing development of an open-source, massively parallel, integrated hydrologic model, Geosci. Model Dev., 13, 1373-1397, https://doi.org/10.5194/gmd-13-1373-2020 2020.

Maxwell, R. M.: A terrain-following grid transform and preconditioner for parallel, large-scale, integrated hydrologic modeling, Advances in Water Resources, 53, 109-117, https://doi.org/10.1016/j.advwatres.2012.10.001, 2013.

Maxwell, R. M., Condon, L. E., Danesh-Yazdi, M., and Bearup, L. A.: Exploring source water mixing and transient residence time distributions of outflow and evapotranspiration with an integrated hydrologic model and Lagrangian particle tracking approach, Ecohydrology, 12, https://doi.org/10.1002/eco.2042Digital, 2019.

Tompson, A. F. B. and Dougherty, D. E.: On the Use of Particle Tracking Methods for Solute Transport in Porous Media, in: Developments in Water Science, edited by: Celia, M. A., Ferrand, L. A., Brebbia, C. A., Gray, W. G., and Pinder, G. F., Elsevier, 227-232, https://doi.org/10.1016/S0167-5648(08)70094-7, 1988.

Tompson, A. F. B. and Gelhar, L. W.: Numerical simulation of solute transport in three-dimensional, randomly heterogeneous porous media, Water Resources Research, 26, 2541-2562, https://doi.org/10.1029/WR026i010p02541, 1990.

Yang, C., Ponder, C., Wang, B., Tran, H., Zhang, J., Swilley, J., Condon, L., and Maxwell, R.: Accelerating the Lagrangian Particle Tracking in Hydrologic Modeling to Continental-Scale, Journal of Advances in Modeling Earth Systems, 15, e2022MS003507, https://doi.org/10.1029/2022MS003507, 2023.